Analyst

PAPER

View Article Online
View Journal | View Issue

Cite this: *Analyst*, 2026, **151**, 1926

Heterojunction-engineered two-dimensional Ti_3C_2–$CoFe_2O_4$ nanozyme with oxidase-like activity for SERS detection of glutathione in human serum

Huiqi Zhu,[a] Ying Chen,[a] Weiqing Yang,[a] Zunxiang Zeng,[a] Yuling Hu *[a] and Ji Zhang*[b]

The inherently weak Raman signals from molecules with small scattering cross-sections pose a significant challenge for surface-enhanced Raman scattering (SERS), a technique that is further limited by its reliance on costly precious metal substrates and exogenous labeling strategies. To address these limitations, this study constructs a Ti_3C_2–$CoFe_2O_4$ heterostructure by anchoring oxidase (OXD)-like $CoFe_2O_4$ nanoparticles (NPs) on two-dimensional (2D) conductive Ti_3C_2 MXene nanosheets. The resulting interface forms a Mott–Schottky junction, which facilitates rapid charge transfer and synergistically enhances both catalytic and SERS performance. Structurally, the 2D Ti_3C_2 framework provides abundant anchoring sites for the uniform dispersion of $CoFe_2O_4$ NPs. This effectively prevents particle aggregation and maximizes the exposure of catalytic active sites, thereby enhancing both stability and catalytic activity. Additionally, the Ti_3C_2–$CoFe_2O_4$ heterojunction effectively suppresses the recombination of charge carriers and promotes the separation of photogenerated charges, generating abundant superoxide anion radicals that oxidize 3,3′,5,5′-tetramethylbenzidine (TMB) for catalytic signal amplification. Therefore, the ingenious combination of nanozymes and SERS technology enables the generation of SERS-active reporters *via* nanozyme-catalyzed reactions, thus avoiding the need for external labeling modifications. The strategy simultaneously enhances Raman signals through the synergistic effect of photoinduced charge transfer and localized surface plasmon resonance. This Ti_3C_2–$CoFe_2O_4$ heterojunction exhibits integrated OXD-like activity and SERS enhancement, enabling sensitive glutathione (GSH) detection in human serum samples. Through catalytic oxidation of TMB to oxidized TMB, a distinct Raman peak emerges at 1615 cm^{-1}, with its intensity reduction quantitatively correlating with GSH concentration *via* competitive reactive oxygen species scavenging. Quantitative analysis demonstrates a linear response range of 0.50–200 $\mu mol\ L^{-1}$ and a detection limit of 0.073 $\mu mol\ L^{-1}$, with serum sample recoveries ranging from 94.7%–115%. This study provides a paradigm for designing non-precious metal nanozyme materials with integrated catalytic and SERS capabilities, demonstrating significant potential for practical applications in clinical diagnostics and biosensing.

Received 18th January 2026,
Accepted 25th February 2026

DOI: 10.1039/d6an00055j

rsc.li/analyst

Introduction

Surface-enhanced Raman scattering (SERS) has become a powerful analytical technique due to its high sensitivity, molecular specificity, and non-destructive characteristics.[1] SERS technology relies on traditional precious metal nanostructures for signal enhancement through localized surface plasmon resonance (LSPR). However, these substrates suffer from aggregation, oxidation, and high costs, limiting their stability and reproducibility in practical applications.[2,3] To circumvent these limitations, non-precious metal substrates have emerged as promising alternatives owing to their excellent chemical stability and cost-effectiveness.[4] Nevertheless, the SERS enhancement of these substrates mainly stems from the chemical mechanism (CM), specifically charge transfer,[5] which is often intrinsically weaker than the electromagnetic mechanism (EM) dominant in precious metals. Particularly, the intrinsically weak Raman signals arising from low scattering cross-sections or improper energy-level alignment of target molecules pose a challenge for direct detection with non-pre-

---

[a] School of Chemistry, Institute of Green Chemistry and Molecular Engineering, Sun Yat-sen University, Guangzhou, 510006, China. E-mail: ceshyl@mail.sysu.edu.cn
[b] Department of Neurosurgery, State Key Laboratory of Oncology in Southern China, Sun Yat-sen University Cancer Center, Collaborative Innovation Center for Cancer Medicine, Guangzhou 510060, China. E-mail: zhangji@sysucc.org.cn

cious metal substrates.[6] Although labeling strategies can be employed to overcome this limitation and achieve the necessary sensitivity,[7] they inevitably introduce cumbersome procedures and signal nonuniformity.[8] To address these challenges, the integration of nanozymes with SERS substrates has been proposed to amplify signals through catalytic reactions, enabling an integrated detection and catalysis platform. In such systems, 3,3′,5,5′-tetramethylbenzidine (TMB) is widely used because its oxidized product (oxTMB) yields strong, reproducible Raman bands for indirect detection and has found broad practical applications.[9,10] Such enzymatic enhancement provides a viable SERS-based approach for indirect small-molecule detection. For instance, Li *et al.* synthesized CeO_2@nanogel/Au nanoparticles (NPs) with enhanced peroxidase (POD)-like activity and established a high-performance SERS platform for the indirect detection of H_2O_2 using its catalytic product as the probe.[11] Similarly, Ruan *et al.* constructed Fe_3O_4@PB@Au@GO_x integrated nanozymes, establishing a colorimetry-SERS dual-mode sensing platform for the indirect detection of glucose and H_2O_2 based on nanozyme-mediated catalytic reactions.[12] Another study reported the design of Co_3O_4@Co–Fe oxide/AuNPs double nanoboxes nanozymes with enhanced POD-like and SERS activities, which enabled the development of a colorimetric-SERS bimodal sensor for the indirect detection of metallothioneins *via* the radical scavenging effect of the protein.[13] These established systems primarily leverage POD-like activity. Recently, advances in nanozyme design have significantly broadened the scope of catalytic SERS beyond POD-like systems, focusing on optimizing catalytic specificity and efficiency. For example, dual-active center nanozymes have been engineered to enhance cascade catalysis through oxygen transfer between spatially separated active sites or to dynamically regulate selectivity by mimicking substrate-induced conformational locking effects in natural enzymes.[14,15] Concurrently, catalytic SERS strategies have progressively extended to other enzyme mimics, including oxidase (OXD)-mimicking materials. More recently, this includes AgNPs@metal–organic framework (MOF)-818 nanozymes exhibiting catechol OXD-like activity for selective dopamine analysis in human urine.[16] Among the developed nanozymes, OXD-like nanozymes offer a distinct advantage over POD-like systems by catalyzing substrate oxidation without requiring exogenous H_2O_2, thereby eliminating instability risks and streamlining workflows. However, studies on non-precious metal nanozymes that integrate high OXD-like activity with efficient SERS enhancement remain scarce. To address this limitation, the rational design of non-precious metal nanozymes with high OXD-like activity aims to enhance the detection of small molecules with low Raman scattering cross-sections.

The key factor governing the synergistic enhancement of catalytic activity and SERS signal intensity in non-precious metal nanozymes lies in the efficiency of interfacial charge transfer. In this regard, heterojunction engineering has emerged as an effective strategy to optimize the interface by facilitating efficient charge transfer and increasing the exposure of active sites.[17] Impressively, semiconducting heterojunctions have shown that rational pairing of dissimilar components can synergistically accelerate charge separation and enrich surface carriers, thereby amplifying both enzyme-like and SERS activity.[18,19] For example, the CuO/TiO_2 p–n heterojunction suppresses carrier recombination and promotes interfacial charge transfer, lowering the SERS detection limit of 4-mercaptobenzoic acid to 1×10^{-10} mol L^{-1}.[20] In addition, our group demonstrated a MoO_{3-x}/CuS heterojunction that integrates SERS and nanozyme capabilities, enabling the sensitive detection of the cerebral infarction biomarker S100B.[21] Further evidence of heterojunction-enhanced catalysis is provided by cobalt ferrite systems. For instance, Guo *et al.* reported that depositing $CoFe_2O_4$ on a conjugated porous organic polymer dramatically boosts its OXD-like activity *via* accelerated electron transfer, enabling ultrasensitive colorimetric detection.[22] Therefore, the construction of a heterojunction with excellent OXD-like activity and SERS enhancement capability provides a novel platform for the highly sensitive detection of small molecules.

As two-dimensional (2D) transition metal carbides, MXenes show significant potential for applications in SERS substrates and catalysis due to their high specific surface area, LSPR effects, and exceptional electrical conductivity.[23,24] However, pristine MXene materials (*e.g.*, Ti_3C_2) exhibit limited SERS enhancement capabilities and inherently lack enzyme-like catalytic properties. Fortunately, the functionalization of nanozyme particles with MXene materials provides a viable pathway to enhance their SERS sensitivity through synergistic effects. As reported in the literature, $CoFe_2O_4$ NPs are magnetic oxides with multiple metal oxidation states and intrinsic enzyme-like activity.[25,26] Nevertheless, $CoFe_2O_4$ NPs exhibit a pronounced tendency to aggregate due to strong magnetic dipole–dipole interactions, which significantly reduces accessible active sites and compromises the catalytic rate.[27,28] Therefore, the integration of $CoFe_2O_4$ nanozymes onto the Ti_3C_2 surfaces seems to be a good choice to further improve the catalytic activity and SERS performance of the heterojunction nanozymes.

In this work, we present a 2D Ti_3C_2–$CoFe_2O_4$ heterojunction with remarkable OXD-like activity and SERS performance. This design achieves a highly dispersed and stable distribution of $CoFe_2O_4$ NPs on the Ti_3C_2 support, fully exposing catalytic active sites. Furthermore, it capitalizes on the excellent metallic conductivity and LSPR effect of Ti_3C_2 to establish a highly conductive interface with $CoFe_2O_4$, effectively forming a Mott–Schottky junction that promotes directional charge transfer and separation. Consequently, the interfacial charge-transfer efficiency is significantly enhanced, realizing a synergistic improvement in both nanozyme catalytic activity and SERS performance. Based on the synergistic enhancement of OXD-like activity at the heterojunction interface, TMB is efficiently oxidized into oxTMB, thereby generating a SERS signal. By leveraging glutathione (GSH)-induced signal quenching and exploiting the competitive scavenging of reactive oxygen species (ROS), a highly sensitive detection strategy for human serum GSH is developed. This strategy offers a novel approach for designing non-precious metal nanozymes that integrate enzymatic catalysis with SERS enhancement, paving the way for advanced biomedical sensing applications.

Experimental sections

Reagents and materials

Titanium aluminium carbide (Ti_3AlC_2) was purchased from Rhawn Co., Ltd. Cobalt dichloride ($CoCl_2 \cdot 6H_2O$) was purchased from Fu Chen Co., Ltd. 3,3′,5,5′-Tetramethylbenzidine (TMB, ≥99%), iron chloride ($FeCl_3 \cdot 6H_2O$), sodium acetate (NaAc), ethylene glycol, ethanol (≥99.8%), hydrogen fluoride (HF, ≥10%, v/v), tetramethylammonium hydroxide (TMAOH, 25 wt%), methanol (≥99.9%), isopropyl alcohol (99.8%), and *p*-benzoquinone (99%) were purchased from Aladdin Co., Ltd. GSH was purchased from Coolaber Technology Co., Ltd. The reduced GSH detection assay kit (G4305-48 T) was purchased from Servicebio. All the raw materials and reagents were of analytical grade and used directly without further purification.

Synthesis of Ti_3C_2 and Ti_3C_2–$CoFe_2O_4$

The Ti_3C_2 material was synthesized according to the method described in a previous report.[29] In a standard synthesis process, 1.0 g of Ti_3AlC_2 powder was initially immersed in 10.0 mL of 10% (v/v) HF at ambient conditions. This mixture was stirred for 5 minutes, resulting in a suspension that was subsequently centrifuged. The solid product was then washed multiple times with deionized water until the pH of the supernatant reached 5–6 to remove excess HF and byproducts. To exfoliate the cleaned bulk material into a sheet-like configuration, the obtained wet sediment was dispersed in a 25 wt% aqueous solution of TMAOH and the mixture was stirred for 24 hours.

The sample from the TMAOH treatment was collected by centrifugation at 6000 rpm for 15 minutes and then redispersed in deionized water at a weight ratio of 1 : 300 (sample : water). By manually shaking this solution for 10 minutes, colloids containing uniformly sized Ti_3C_2 sheets terminated with $Al(OH)_4^-$ were formed. To remove unexfoliated particles, the colloid was centrifuged at 3500 rpm for 15 minutes. The supernatant was collected and dried under vacuum at 60 °C for 12 hours to obtain the final product of delaminated Ti_3C_2.

The preparation of Ti_3C_2–$CoFe_2O_4$ composites were as follows. The Ti_3C_2–$CoFe_2O_4$ composites were synthesized with controlled mass ratios by systematically varying the Ti_3C_2 MXene loading while maintaining identical precursor inputs for $CoFe_2O_4$ formation. Specifically, 5 mg of Ti_3C_2 nanosheets dispersed in 30 mL ethylene glycol with 2 mmol $FeCl_3 \cdot 6H_2O$ and 1 mmol $CoCl_2 \cdot 6H_2O$ yielded the 1 : 1 Ti_3C_2–$CoFe_2O_4$ composite. Proportional increases to 10 mg and 15 mg of Ti_3C_2 under identical precursor conditions and solvent volume produced the 1 : 2 and 1 : 3 Ti_3C_2–$CoFe_2O_4$ composites, respectively.

All mixtures underwent ultrasonication followed by hydrothermal treatment at 180 °C for 24 hours to crystallize the heterostructures. After being allowed to cool naturally to room temperature, the resulting black precipitate was collected by filtration and washed sequentially with absolute ethanol and deionized water several times. The final product was dried in a vacuum oven at 60 °C for 12 hours prior to use. The nanocomposite preparation procedure is illustrated in Scheme S1. Pure $CoFe_2O_4$ was prepared following the same procedure but without the addition of Ti_3C_2.

Characterization

Scanning electron microscopy (SEM, Bruker Gemini500 and SU8010) and transmission electron microscopy (TEM, JEM-2010 HR) were employed to characterize the morphology of the synthesized samples. Powder X-ray diffraction (XRD) measurements were performed on a SmartLab X-ray Powder Diffractometer (Rigaku, Japan). X-ray photoelectron spectroscopy (XPS) was carried out using a Thermo Scientific Nexsa to determine the compositional and valence state information of the prepared samples. The contents of Fe and Co in the prepared Ti_3C_2–$CoFe_2O_4$ samples were determined by inductively coupled plasma optical emission spectrometry (ICP-OES) with an Agilent 720ES ICP-OES spectrometer. Ultraviolet–visible-near-infrared (UV-vis-NIR) and ultraviolet-visible (UV-vis) absorbance spectra were measured by a Shimadzu UV-3600 spectrophotometer (Shimadzu, Japan). Zeta potential (ζ) was measured to determine the surface charge of the materials (EliteSizer). The photoluminescence spectra were recorded using a fluorescence spectrophotometer (Shimadzu, Japan) at an excitation wavelength of 244 nm. Diffuse reflectance spectra were recorded using UV-vis diffuse reflectance spectroscopy (UV-vis DRS, PerkinElmer Lambda 950) in the range of 200–800 nm. Mott–Schottky (M–S) measurements were performed in 0.1 mol L^{-1} Na_2SO_4, while electrochemical impedance spectroscopy (EIS) was conducted in 5 mmol L^{-1} $K_3[Fe(CN)_6]/K_4[Fe(CN)_6]$ and 0.1 mol L^{-1} KCl, using an electrochemical workstation (CHI-660E, Shanghai, China) with a standard three-electrode system comprising a glassy carbon working electrode, a platinum counter electrode and an Ag/AgCl reference electrode. Raman measurements were performed on liquid samples using an RM5 microscopy Raman spectrometer at an excitation laser wavelength of 633 nm. A 10× objective lens with an accumulation time of 10 seconds was used for SERS signal collection.

Evaluation of oxidase-like property of Ti_3C_2–$CoFe_2O_4$

The verification of the Ti_3C_2–$CoFe_2O_4$ OXD-like activity was as follows: 100.0 µL 5 mmol L^{-1} TMB solution and the prepared Ti_3C_2–$CoFe_2O_4$ dispersion (100.0 µL, 1 mg mL^{-1}) were mixed with the buffer (HAc–NaAc, 800.0 µL, 0.1 mol L^{-1}, pH = 3.0). After 10 minutes, the spectrum was measured using UV-vis spectroscopy.

SERS measurements of GSH

GSH solutions (50.0 µL) at various concentrations, TMB (5 mmol L^{-1}, 20.0 µL), Ti_3C_2–$CoFe_2O_4$ (50.0 µL, 1 mg mL^{-1}), and buffer (0.1 mol L^{-1} HAc–NaAc, pH = 3.0) were mixed to a final volume of 200 μL. After incubation for 10 minutes at 35 °C, the SERS spectrum was measured. The analytical signal was calculated as the difference in SERS intensity between the samples with and without GSH. All experiments were performed in triplicate.

Analysis of serum samples

Serum samples were provided by the Affiliated Cancer Hospital of Sun Yat-sen University. The analytical procedure was as follows: the samples were collected and diluted 20-fold with a pH 3.0 buffer solution before proceeding with SERS analysis. The diluted serum samples (50.0 μL) were mixed with TMB (5 mmol L^{-1}, 20.0 μL), Ti_3C_2–$CoFe_2O_4$ (50.0 μL, 1 mg mL^{-1}), and buffer (0.1 M HAc–NaAc, pH = 3.0) to obtain a total volume of 200 μL. After incubation for 10 minutes at 35 °C, the SERS spectrum was measured. The SERS signals were recorded on a spectrometer under 633 nm laser excitation with an accumulation time of 10 seconds. For comparison, the GSH levels in human serum were also determined by the standard method using a Reduced GSH Detection Assay Kit (Servicebio, G4305-48 T), which is based on Ellman's method.

Results and discussion

Characterization of Ti_3C_2–$CoFe_2O_4$

The morphology and microstructure of the as-prepared Ti_3C_2–$CoFe_2O_4$ composite (with a 1 : 2 mass ratio, used hereafter unless otherwise stated) were investigated by SEM and TEM. After TMAOH etching, Ti_3C_2 exhibited ultrathin lamellar nanostructures (Fig. 1A and S1A, B), which provided abundant active sites for probe molecules and thereby significantly enhanced the SERS detection sensitivity. Bare $CoFe_2O_4$ formed spherical NPs with an average size of approximately 100 nm (Fig. 1B and S1C), but exhibited severe agglomeration due to magnetic dipole–dipole interactions. In contrast, after anchoring $CoFe_2O_4$ onto Ti_3C_2 nanosheets, magnetic agglomeration was significantly suppressed while the particulate morphology was retained (Fig. 1C and S1D). Moreover, EDS elemental mapping (Fig. 1E–J) demonstrated the homogeneous distribution of Co, Fe, O, C, and Ti, confirming the successful construction of the composite heterostructure. Quantitative analysis by ICP-OES indicated that the mass fractions of Fe and Co were 36.43% and 17.34%, respectively, corresponding to a molar ratio of approximately 2.22 : 1. This ratio is consistent with the theoretical stoichiometric ratio of $CoFe_2O_4$, and the loading content of $CoFe_2O_4$ was determined to be 72.79 wt%. HRTEM imaging (Fig. 1D) showed the clear deposition of $CoFe_2O_4$ on Ti_3C_2. The measured interplanar spacing of 0.218 nm corresponded to the Ti_3C_2 (105) plane.[30,31] The spacing of 0.257 nm was attributed to the $CoFe_2O_4$ (311) plane. The XRD patterns of the $CoFe_2O_4$ and Ti_3C_2–$CoFe_2O_4$ composites (Fig. S2) were consistent with the standard $CoFe_2O_4$ structure (JCPDS no. 22-1086), and the prominent diffraction peaks corresponded to the (220), (311), (400), (511), and (440) planes.[32] These collective findings confirmed the formation of heterojunctions between the two components, which facilitated faster charge transport.

XPS is an important technology for determining the binding energy of elements, which can be used to estimate the charge transfer behavior of heterostructures.[33] Fig. 2 presented the XPS spectra of $CoFe_2O_4$ and Ti_3C_2–$CoFe_2O_4$. Fig. 2A–D collectively revealed the elemental composition (C, O, Ti, Co, Fe) and chemical bonding states (C–Ti, C–C, C–F, Ti–O) in the Ti_3C_2–$CoFe_2O_4$ composite.[34–37] Moreover, the XPS analysis provided critical insights into the chemical states and interfacial interactions in the Ti_3C_2–$CoFe_2O_4$ composite. For the pure $CoFe_2O_4$ sample, multiple peaks were detected in the Co 2p spectrum (Fig. 2E), reflecting the characteristics of Co species in different lattice sites. The peaks at 780.2/795.6 eV corre-

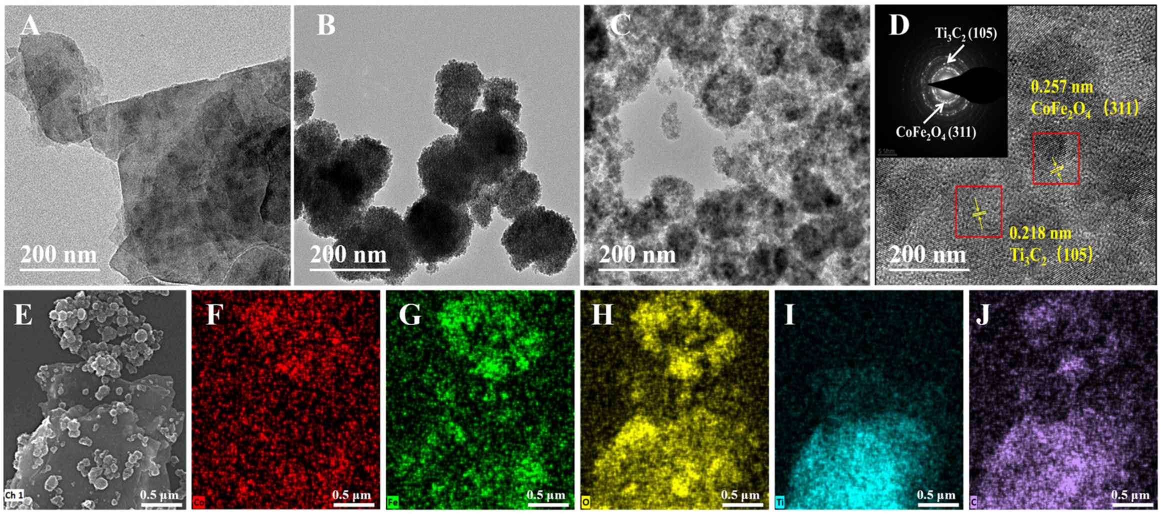

Fig. 1 TEM images of (A) Ti_3C_2, (B) $CoFe_2O_4$, (C) Ti_3C_2–$CoFe_2O_4$. (D) HRTEM images of Ti_3C_2–$CoFe_2O_4$ (inset: SAED pattern of Ti_3C_2–$CoFe_2O_4$). (E) SEM of Ti_3C_2–$CoFe_2O_4$ and EDS mapping of (F) Co, (G) Fe, (H) O, (I) Ti and (J) C of Ti_3C_2–$CoFe_2O_4$.

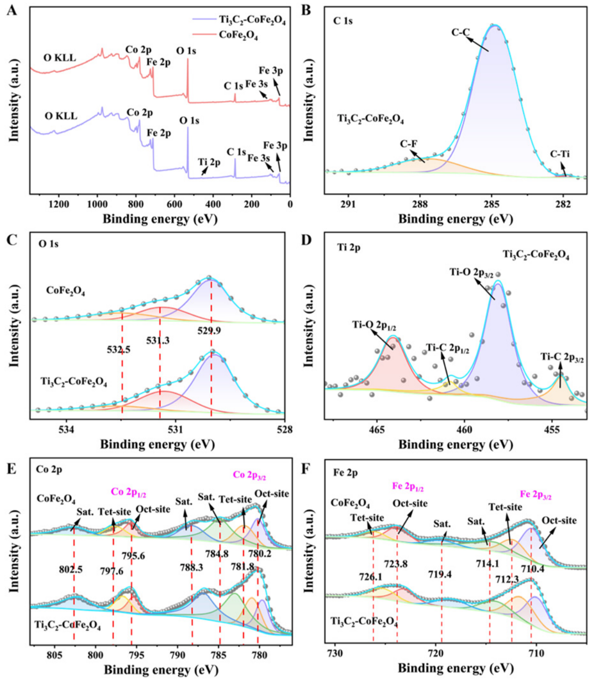

Fig. 2 XPS analyses of $CoFe_2O_4$ and Ti_3C_2–$CoFe_2O_4$: (A) full-scan XPS spectra; (B) C 1s; (C) O 1s; (D) Ti 2p; (E) Co 2p; (F) Fe 2p.

sponded to Co^{2+} $2p_{3/2}/2p_{1/2}$ in octahedral sites, while those at 781.8/797.6 eV corresponded to Co^{2+} $2p_{3/2}/2p_{1/2}$ in tetrahedral sites. The Fe 2p spectrum (Fig. 2F) also revealed Fe species in different coordination environments. The peaks at 710.4/723.8 eV corresponded to Fe^{3+} $2p_{3/2}/2p_{1/2}$ in octahedral sites, and those at 712.3/726.1 eV corresponded to Fe^{3+} $2p_{3/2}/2p_{1/2}$ in tetrahedral sites.[37] In contrast, the Ti_3C_2–$CoFe_2O_4$ composite material displayed slight but consistent binding energy downshifts across O 1s, Co 2p, and Fe 2p spectra compared to pure $CoFe_2O_4$. This negative shift indicated the electron transfer from Ti_3C_2 to $CoFe_2O_4$, driven by Fermi level equilibration at the heterojunction interface. The alignment of energy levels facilitated thermodynamic equilibrium, confirming the formation of a Mott–Schottky junction at the Ti_3C_2–$CoFe_2O_4$ interface. This electronic interaction underpinned the enhanced charge separation observed in catalytic performance.

The oxidase-like property of Ti_3C_2–$CoFe_2O_4$

Following characterization, the OXD-like activity of Ti_3C_2–$CoFe_2O_4$ composites were assessed by UV-vis and SERS monitoring of TMB oxidation. Ti_3C_2–$CoFe_2O_4$ composites with different ratios were tested for their ability to catalyze TMB oxidation, with SERS signals at 1615 cm^{-1} (assigned to ring stretching and C–H bending modes of the single-electron oxidation product)[38] and UV absorption at 652 nm monitored. The 1 : 2 Ti_3C_2–$CoFe_2O_4$ showed the most intense Raman peak at 1615 cm^{-1} and the highest absorbance at 652 nm (Fig. 3A and B). Meanwhile, the absorbance of the Ti_3C_2–$CoFe_2O_4$ heterojunction with TMB increased in a time-dependent manner until TMB was completely oxidized in 10 minutes (Fig. S3). Such excellent catalytic performance was not observed for the simply physically blended Ti_3C_2/$CoFe_2O_4$, which only exhibited

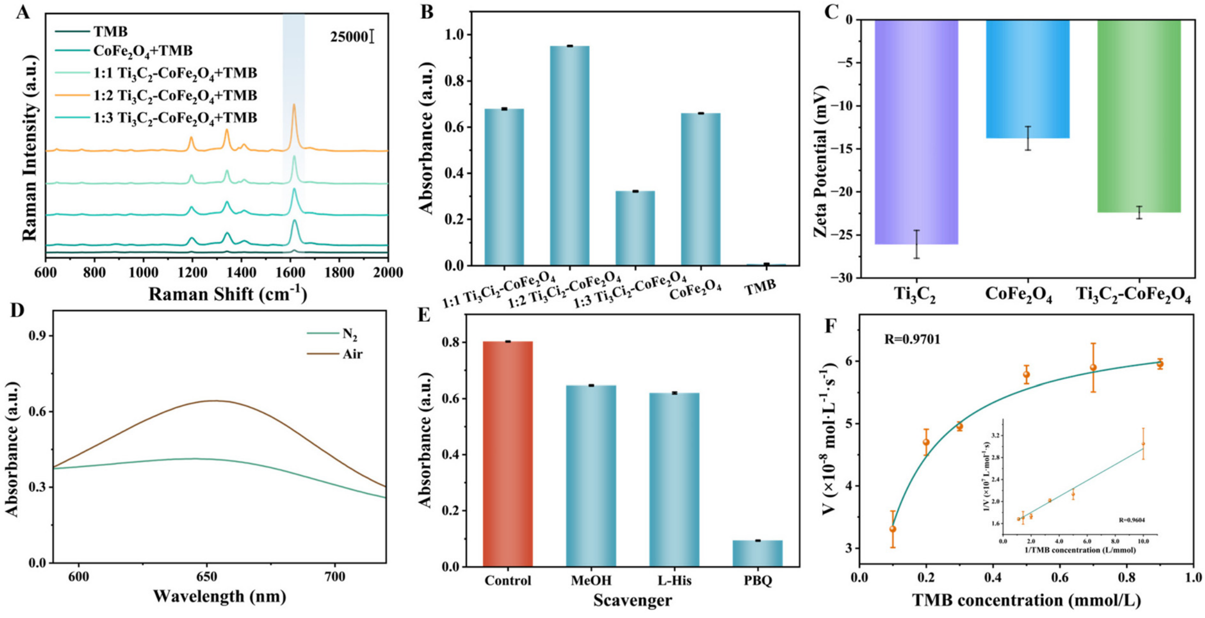

Fig. 3 (A) SERS spectra of TMB with $CoFe_2O_4$ and Ti_3C_2–$CoFe_2O_4$ composites at different mass ratios. (B) UV-vis absorbance at 652 nm for TMB, $CoFe_2O_4$ with TMB, and TMB with Ti_3C_2–$CoFe_2O_4$ composites at different mass ratios. (C) Zeta potential spectra of Ti_3C_2, $CoFe_2O_4$ and Ti_3C_2–$CoFe_2O_4$. (D) Absorption spectra of TMB with Ti_3C_2–$CoFe_2O_4$ system under different gaseous conditions (air, N_2). (E) Absorbance of TMB at 652 nm in the Ti_3C_2–$CoFe_2O_4$ using different scavengers. (F) Michaelis–Menten equation of Ti_3C_2–$CoFe_2O_4$ material at different concentrations of TMB (inset: Lineweaver–Burk plots of the velocity *versus* varying concentrations of TMB).

weak and broad oxTMB absorption peaks in the reaction system (Fig. S4). This superior performance may stem from charge transfer between Ti_3C_2 and $CoFe_2O_4$. Zeta potential characterization (Fig. 3C) revealed that a more negative surface charge was exhibited by the Ti_3C_2–$CoFe_2O_4$ composite compared to pure $CoFe_2O_4$ following incorporation of negatively charged Ti_3C_2. This enhanced negative charge facilitated electrostatic interactions with positively charged TMB, thereby improving OXD-like activity. Subsequent optimization of catalytic performance was conducted through systematic variation of pH, temperature, and component concentrations (Fig. S5). Optimal reaction conditions were identified as pH 3.0, 35 °C, 0.25 mg mL^{-1} composite concentration, and 0.5 mmol L^{-1} TMB concentration.

Additionally, to explore the catalytic mechanism of the Ti_3C_2–$CoFe_2O_4$ material, the effect of oxygen on its OXD-like activity was investigated. As shown in Fig. 3D, the absorbance peak at 652 nm decreased significantly when N_2 was introduced into the reaction system, suggesting that O_2 was essential for the OXD-like activity of Ti_3C_2–$CoFe_2O_4$. Furthermore, different radical scavengers were used to identify the radicals produced during the catalytic reaction of Ti_3C_2–$CoFe_2O_4$. The addition of *p*-benzoquinone (PBQ), a superoxide anion radical ($O_2^{\bullet-}$) scavenger, caused a significant decrease in the absorbance at 652 nm, indicating strong inhibition of the catalytic activity of Ti_3C_2–$CoFe_2O_4$. In contrast, methanol (MeOH), a hydroxyl radical scavenger, and L-histidine (L-His), a singlet oxygen scavenger, caused only slight decreases in the absorbance when added to the system. These results confirmed that $O_2^{\bullet-}$ played a primary role in the catalytic system and demonstrated that Ti_3C_2–$CoFe_2O_4$ generates $O_2^{\bullet-}$ by catalyzing O_2 (Fig. 3E).

The steady-state kinetics of the Ti_3C_2–$CoFe_2O_4$ were calculated using the Michaelis–Menten equation ($V = V_{\max} \times [S]/(K_m + [S])$) and the Lineweaver–Burk equation ($1/V = K_m/V_{\max} \times [1/S] + 1/V_{\max}$), based on changes in TMB concentration while keeping other concentrations constant.[39] This further confirmed the catalytic mechanism, where $V_{\max}$ represents the maximum reaction rate, $[S]$ is the substrate concentration, and K_m is the Michaelis–Menten constant. Fig. 3F illustrates the relationship between reaction rate and substrate concentration, and the inset in Fig. 3F shows the linear relationship obtained by double reciprocal transformation of the Michaelis–Menten equation. Using the Michaelis–Menten calculation method, the K_m value for TMB and the maximum reaction rate $V_{\max}$ of the system were determined. The Ti_3C_2–$CoFe_2O_4$ nanozyme has the smallest K_m value for TMB (Table S1), indicating the highest affinity and best catalytic performance among the materials compared.

Synergistic mechanism for Ti_3C_2–$CoFe_2O_4$ oxidase-like catalysis and SERS enhancement

The synergistic enhancement mechanism of OXD-like activity and SERS signals for the Ti_3C_2–$CoFe_2O_4$ heterojunction was explored by measuring the UV-vis DRS spectra of $CoFe_2O_4$ and Ti_3C_2–$CoFe_2O_4$, as well as the Mott–Schottky plot of $CoFe_2O_4$ (Fig. S6 and S7). Ti_3C_2–$CoFe_2O_4$ exhibits a narrowed bandgap compared to the pristine $CoFe_2O_4$ (Fig. S6), which enhances visible light absorption and facilitates the generation of photogenerated electron–hole pairs for efficient charge separation. To evaluate the contribution of light, the catalytic oxidation of TMB was monitored by UV-vis absorption at 652 nm under dark and ambient light conditions. The results showed accelerated oxTMB formation under ambient light (Fig. S8), supporting a photo-assisted charge transfer process. Based on these findings, Fig. 4A depicts a plausible mechanism for this synergistic enhancement. The SERS enhancement of the heterojunction involves both interfacial charge transfer through the Mott–Schottky junction and electromagnetic contribution from Ti_3C_2 LSPR. When metallic Ti_3C_2 (Fermi level $E_f = -0.04$ V *vs.* normal hydrogen electrode (NHE)[40]) contacts the p-type semiconductor $CoFe_2O_4$, the E_f of $CoFe_2O_4$ is well-documented to be closely aligned with its valence band (VB).[41] Driven by the Fermi level gradient from higher to lower energy, spontaneous electron transfer occurs from Ti_3C_2 to $CoFe_2O_4$ (as corroborated by the XPS results in Fig. 2) until the system reaches a unified Fermi level at equilibrium. This charge transfer process creates positive charge centers on the Ti_3C_2 side and negative charge centers on the $CoFe_2O_4$ side at the interface, thereby establishing a built-in electric field pointing from Ti_3C_2 to $CoFe_2O_4$. Interfacial electronic coupling between Ti_3C_2 and $CoFe_2O_4$ establishes a rectifying contact by forming a Mott–Schottky junction, which generates abundant ROS-mediated oxidation sites.[42,43] Under light irradiation, electrons in the VB of $CoFe_2O_4$ are excited to the conduction band (CB), generating electron–hole pairs. The built-in field facilitates the rapid transfer of these photogenerated electrons from the CB of $CoFe_2O_4$ to Ti_3C_2, where Ti_3C_2 acts as an electron reservoir to stabilize charge separation and suppress recombination. Concurrently, the LSPR effect of Ti_3C_2 under laser excitation generates hot electrons.[44] UV-vis-NIR spectra confirm the LSPR response of Ti_3C_2 and its retention in the heterojunction, as evidenced by the NIR peak shift and broadening after coupling with $CoFe_2O_4$ (Fig. S9). These hot electrons can inject into the CB of $CoFe_2O_4$ under photoexcitation *via* Landau damping. This bidirectional electron transfer, coupled with the built-in field-driven carrier migration, effectively suppresses charge recombination and achieves efficient separation of photogenerated electrons and holes. It thereby lays the critical foundation for the two core functionalities of the heterojunction, which are enhanced OXD-like activity and amplified SERS enhancement. The OXD-like activity is realized through a ROS-mediated catalytic oxidation pathway. Specifically, electrons accumulated on Ti_3C_2 reduce dissolved oxygen to generate $O_2^{\bullet-}$, and these radicals further convert low Raman-active TMB into high Raman-active oxTMB.[45,46] The SERS enhancement relies on a synergistic effect of CM and EM. The CM originates from the photoinduced charge transfer (PICT) between $CoFe_2O_4$ and adsorbed TMB, where holes in the VB of $CoFe_2O_4$ are transferred to TMB molecules. This charge transfer process not only increases the molecular polarizability of TMB and its oxidized products but also promotes the formation of $TMB^{\bullet+}$

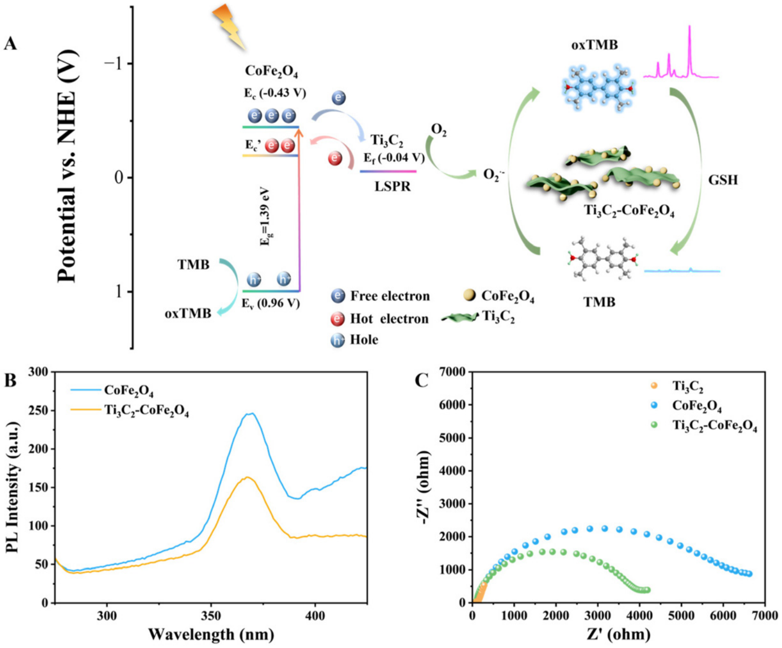

Fig. 4 (A) Synergistic enhancement of OXD-like activity and SERS signals by Ti_3C_2–$CoFe_2O_4$ heterojunction. (B) PL spectra of $CoFe_2O_4$ and Ti_3C_2–$CoFe_2O_4$ composites. (C) EIS Nyquist plots of Ti_3C_2, $CoFe_2O_4$ and Ti_3C_2–$CoFe_2O_4$ composites.

radicals and oxTMB, which are species with larger Raman cross-sections, thereby significantly boosting the CM for SERS.[47] Meanwhile, the localized electromagnetic field generated by the LSPR effect of Ti_3C_2 under light excitation affords an auxiliary contribution to the EM and further amplifies the Raman signal of oxTMB.[48] Notably, Ti_3C_2–$CoFe_2O_4$ establishes a quantifiable signal transduction pathway by catalyzing the conversion of O_2 to $O_2^{\bullet-}$ for TMB oxidation. GSH competes with TMB for $O_2^{\bullet-}$ consumption, which in turn reduces the production of oxTMB.[49] Based on this mechanism, a SERS signal attenuation model is constructed to achieve sensitive detection of GSH. Collectively, the optimized interfacial band alignment and electronic coupling in the Ti_3C_2–$CoFe_2O_4$ heterojunction enable efficient charge separation and utilization. These features synergistically boost OXD-like catalytic activity and amplify SERS enhancement through oxidation mediated by ROS, chemical enhancement driven by PICT, and electromagnetic enhancement derived from LSPR.

The spatial charge separation efficiency was examined by the photoluminescence (PL) technique. As shown in Fig. 4B, the pristine $CoFe_2O_4$ presented a broad and intense emission peak centered around 368 nm, originating from the band-gap recombination of photogenerated electrons and holes. The incorporation of Ti_3C_2 resulted in a significant reduction in photoluminescence intensity from the composite, demonstrating effective suppression of charge recombination and enhanced charge separation efficiency. To gain deeper insight into charge carrier dynamics, electrochemical impedance spectroscopy (EIS) analysis was performed. Results showed the Ti_3C_2–$CoFe_2O_4$ composite exhibited a smaller Nyquist plot diameter than $CoFe_2O_4$, indicating lower impedance and charge transfer resistance (Fig. 4C). This reflected the high conductivity of Ti_3C_2 and the faster interfacial charge-transfer kinetics of the formed heterojunction.

Quantitative detection of GSH

The Ti_3C_2–$CoFe_2O_4$ nanocomposite exhibits both OXD-like activity and SERS enhancement, enabling sensitive GSH detection through a redox-mediated signal transduction mechanism. As an OXD-like nanozyme, the Ti_3C_2–$CoFe_2O_4$ catalyzes TMB oxidation to blue oxTMB without H_2O_2, generating strong SERS signals. Upon GSH introduction, the antioxidant properties of GSH scavenge $O_2^{\bullet-}$ and reduce oxTMB back to TMB, leading to decreased SERS intensity. This strategy enables sensitive and selective GSH detection by combining catalytic signal amplification with SERS, offering clinical potential for monitoring oxidative stress biomarkers.

A SERS strategy for the quantitative analysis of GSH was successfully established under optimal experimental conditions. As depicted in Fig. 5A, the SERS intensity at 1615 cm^{-1} decreased as the GSH concentration increased. The standard curve was plotted based on the relationship between the 1615 cm^{-1} intensity and the GSH concentration (Fig. 5B). The regression equation was $\Delta I = 22\,772.99 \log C_{[GSH]} + 28\,412.67$ with a linear correlation coefficient (R) of 0.9949. The limit of detection was 0.073 μmol L^{-1}, and the linear range extended from 0.50 to 200 μmol L^{-1}. Compared to other GSH detection methods (Table S2), this SERS strategy shows higher sensitivity and a broader linear range.

To evaluate the selectivity and interference resistance of the proposed SERS detection method for GSH, the method was exposed to several potential human serum interfering sub-

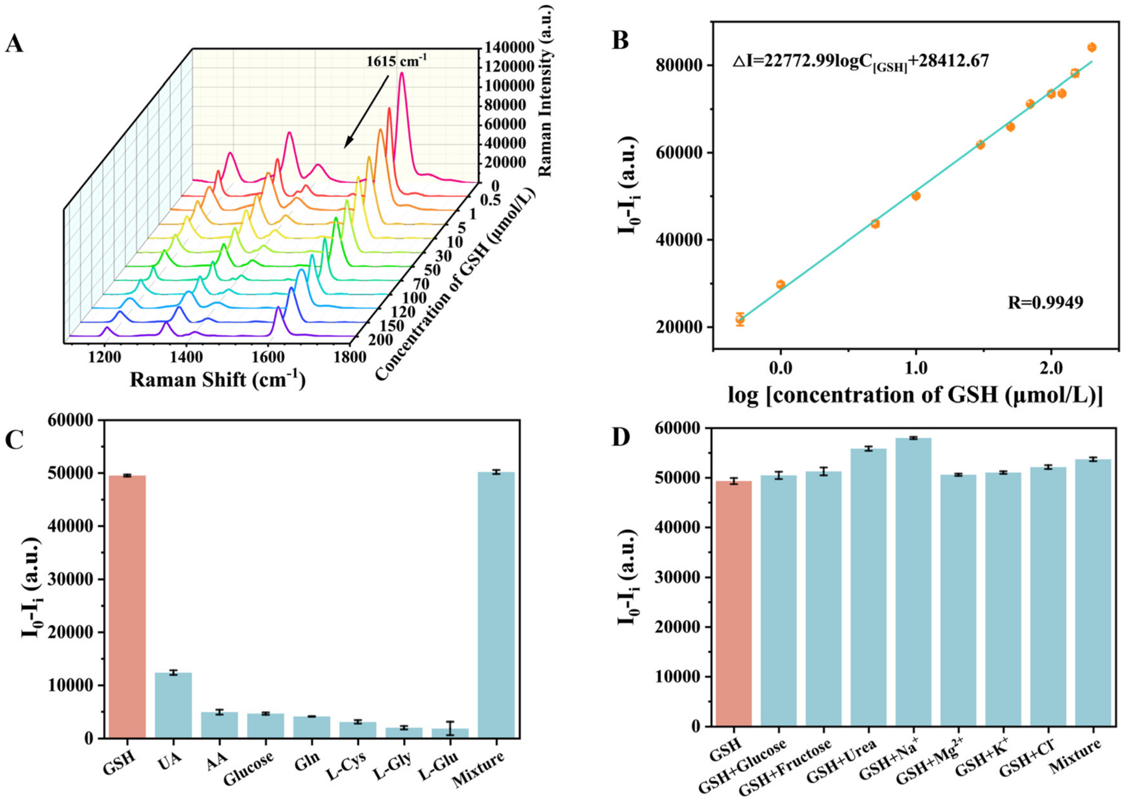

Fig. 5 (A) SERS spectra of GSH with different concentrations. (B) The linear relationship between SERS signal changes at 1615 cm^{-1} and the concentrations of GSH. $\Delta I = I_0 - I_i$, I_0: the initial SERS intensity at 1615 cm^{-1} of oxTMB without GSH; I_i: the SERS intensity at 1615 cm^{-1} of oxTMB with various levels of GSH. (C) The selectivity investigation with various substances, including GSH (10.0 μmol L^{-1}), UA (100 μmol L^{-1}), ascorbic acid (100.0 μmol L^{-1}), glucose (5.00 mmol L^{-1}), glutamine (100 μmol L^{-1}), L-cysteine (2.00 μmol L^{-1}), L-glycine (100 μmol L^{-1}), L-glutamic acid (100 μmol L^{-1}), and valine (100 μmol L^{-1}). (D) The influence of potential interferent substances on the SERS detection method for GSH. The GSH concentration was 10.0 μmol L^{-1}, while glucose, fructose, urea, Na$^+$, Mg^{2+}, K$^+$, and Cl$^-$ were each at 5 mmol L^{-1}.

stances. The selectivity experiment results are shown in Fig. 5C. A significant SERS signal reduction was observed for GSH, while other interfering substances exhibited almost no SERS signal reduction. Additionally, monitoring results of key interfering substances are presented in Fig. 5D. When the concentrations of these substances were 500 times those of GSH, they had almost no effect on the SERS intensity. Notably, the proposed SERS detection system operates optimally at pH 3.0, which is lower than the typical pH range (4.0–5.0) suitable for peroxidases. Consistent with previous research,[50] such strongly acidic conditions (pH < 3.5) can enhance the stability of oxidation-related species while mitigating undesirable side reactions and competitive adsorption from interfering substances, thereby further contributing to the excellent interference resistance. These results indicate that the developed method shows excellent sensitivity, selectivity, and interference resistance, enabling reliable GSH detection in human serum. The stability and repeatability of Ti_3C_2–$CoFe_2O_4$ were also tested due to the critical role in practical application. Time-dependent SERS measurements of TMB on the Ti_3C_2–$CoFe_2O_4$ composite over 40 minutes gave a relative standard deviation (RSD) of 1.6% (Fig. S10), verifying excellent temporal SERS signal stability. As shown in Fig. S11, the corresponding SERS intensity of the peak at 1615 cm^{-1} was collected, indicating that Ti_3C_2–$CoFe_2O_4$ still retained high SERS activity and OXD-like activity after being stored at 4 °C for 35 days with an RSD of 3.6%. As manifested in Fig. S12, the SERS signals of 10 different batches of Ti_3C_2–$CoFe_2O_4$ substrates were detected. It can be observed that the intensity of the peak was essentially stable with the RSD of 1.5%. This analytical strategy exhibited excellent stability and batch reproducibility, thus laying a solid foundation for the subsequent detection of GSH in clinical samples.

Clinical serum sample analysis

To validate the practical application of the proposed SERS detection method for GSH, human serum samples were analyzed that had been collected from hepatocellular carcinoma patients and myocarditis patients. The results were compared with those from the Ellman's method. As shown in Table S3, the GSH levels in 10 human serum samples detected by this method were consistent with the values provided by the standard method but with more convenient operation and lower cost. The relative error between the two methods was within ±5.5%. Meanwhile, the RSD was below 9.7%, indicating its accuracy and reliability in detecting GSH in real serum

Table 1 Detection of GSH concentration in human serum samples

Samples	SERS method (μmol L^{-1})	Added (μmol L^{-1})	Found (μmol L^{-1})	Recovery (%)	RSD (%, n = 3)
Serum 1	35.5	10.0	46.7	112	5.0
		30.0	70.0	115	1.6
		50.0	85.1	99.2	4.0
Serum 2	14.6	10.0	25.0	104	0.7
		20.0	34.1	97.5	5.4
		30.0	43.0	94.7	7.6
Serum 3	25.4	20.0	46.7	111	5.0
		30.0	54.6	100	2.7
		50.0	73.1	97.2	3.7

samples. Additionally, a recovery test was performed by spiking different GSH concentration gradients into three selected serum samples. The recoveries ranged from 94.7% to 115% with RSD less than 7.6% (Table 1). These results suggest that the method has broad application prospects for detecting GSH in human serum.

Conclusions

In summary, a novel 2D Ti_3C_2–$CoFe_2O_4$ nanozyme was constructed through heterojunction engineering, successfully integrating high OXD-like activity and intrinsic SERS enhancement into a single non-precious metal platform. This design overcomes the challenge of coupling efficient nanozyme catalysis with sensitive, label-free detection in complex biological matrices. The key innovation lies in the markedly enhanced interfacial charge transfer, which under photoexcitation promotes charge separation and hot electron injection. This process leads to a significant enhancement in ROS generation and a strong SERS signal from the catalytic product, synergistically amplified by PICT and LSPR of the heterojunction. This mechanism enabled the development of a label-free sensing platform for GSH detection in human serum, exhibiting ultrahigh sensitivity, a wide linear range, excellent anti-interference capability, and reliable accuracy validated against the Ellman's method. The heterojunction engineering strategy presented herein provides a versatile and generalizable paradigm for designing next-generation multifunctional nanozymes. Capitalizing on the excellent anti-interference capability, this platform holds great potential for multiplexed biomarker detection in complex biological fluids such as saliva and urine. Furthermore, through rational modulation of heterojunction components, this strategy can be extended to monitor diverse redox-active biomolecules, offering a powerful tool for precision diagnostics and rapid clinical analysis.

Author contributions

Huiqi Zhu: conceptualization, investigation, writing – original draft. Ying Chen: data curation. Weiqing Yang: visualization. Zunxiang Zeng: investigation. Yuling Hu: conceptualization, writing – review & editing, resources, and supervision. Ji Zhang: resources, project administration.

Conflicts of interest

There are no conflicts to declare.

Data availability

The data are available from the corresponding author on reasonable request.

Supplementary information (SI) is available. Supplementary material: Additional information on steady-kinetic analysis; band edge position determination for $CoFe_2O_4$; SEM and spectral characterization; optimization of OXD-like catalytic conditions; SERS stability and reproducibility tests; kinetic parameter comparison; GSH detection method evaluation; clinical serum sample analysis. See DOI: https://doi.org/10.1039/d6an00055j.

Acknowledgements

This research was funded by the National Natural Science Foundation of China (No. 22574176, 22074162).

References

1 S. Jin, D. Zhang, B. Yang, S. Guo, L. Chen and Y. M. Jung, *Analyst*, 2024, **149**, 11–28.
2 T. Endo, H. Yamada and K. Yamada, *Micromachines*, 2020, **11**, 936.
3 Y. Qiu, C. Kuang, X. Liu and L. Tang, *Sensors*, 2022, **22**, 4889.
4 L. Chen, H. Liu, J. Gao, J. Wang, Z. Jin, M. Lv and S. Yan, *Nanomaterials*, 2024, **14**, 1654.
5 X. Wang, E. Zhang, H. Shi, Y. Tao and X. Ren, *Analyst*, 2022, **147**, 1257–1272.
6 D. P. Dos Santos, M. M. Sena, M. R. Almeida, I. O. Mazali, A. C. Olivieri and J. E. L. Villa, *Anal. Bioanal. Chem.*, 2023, **415**, 3945–3966.
7 I. B. Becerril-Castro, I. Calderon, J. Ockova, M. Liebel, N. F. van Hulst, V. Giannini and R. A. Alvarez-Puebla, *ACS Appl. Mater. Interfaces*, 2022, **14**, 57165–57170.
8 L. Li, X. Cao, T. Zhang, Q. Wu, P. Xiang, C. Shen, L. Zou and Q. Li, *Foods*, 2022, **11**, 2165.
9 Y. Wang, S. Zhang, Q. Yin, J. Wei, J. Liu and L. Wu, *Trends Anal. Chem.*, 2026, **196**, 118632.
10 Z. Li, M. Shen, F. Meng, Y. Zhang, W. Duan, C. Hou and M. Zhang, *Small*, 2025, **21**, 2501976.
11 Y. Li, Y. Zhang, H. Jiang, M. Qi, X. Zhang, B. Zhu and L. Han, *Microchem. J.*, 2023, **195**, 109467.
12 S. Ruan, S. Chen, Y. Tu, Y. Liu, R. You, Q. Lin and Y. Lu, *Microchem. J.*, 2024, **205**, 111377.

13 Y. Long, J. Li, F. Shi, Y. Xue, Y. Wang, Z. Yang and J. Li, *Anal. Chem.*, 2025, **97**, 22279–22287.

14 H. Shen, S. Chen, S. Mo, H. Huang, H. Liang, J. Zhang, Z. Xu, W. Liu and Y. Liu, *Adv. Funct. Mater.*, 2025, **35**, 2418360.

15 H. Shen, H. Huang, B. Shu, P. Zhang, Z. Xu, W. Liu, S. Chen and Y. Liu, *Adv. Mater.*, 2025, e21184.

16 S. Liu, G. Li and Y. Hu, *Talanta*, 2026, **298**, 128907.

17 D. Wu, Q. Liang, H. Si, X. Yan, H. Huang, Z. Li and Z. Kang, *J. Mater. Chem. A*, 2022, **10**, 24519–24528.

18 L. Jiang, R. Hu, A. Wang, L. Mei and J. Feng, *Sens. Actuators, B*, 2023, **382**, 133491.

19 H. Zhang, Y. Tang, W. Wang, D. Yu, L. Yang, X. Jiang, W. Song and B. Zhao, *Food Chem.*, 2024, **431**, 137163.

20 D. Yu, L. Xu, H. Zhang, J. Li, W. Wang, L. Yang, X. Jiang and B. Zhao, *Chin. Chem. Lett.*, 2023, **34**, 107771.

21 Y. Chen, J. Zhang, Y. Li, G. Li and Y. Hu, *Anal. Chem.*, 2024, **96**, 17711–17719.

22 X. Guo, F. Yang, L. Jing, J. Li, Y. Li, R. Ding, B. Duan and X. Zhang, *J. Hazard. Mater.*, 2022, **431**, 128621.

23 Y. Gogotsi and B. Anasori, *ACS Nano*, 2019, **13**, 8491–8494.

24 Z. Said, A. K. Pandey, A. K. Tiwari, B. Kalidasan, F. Jamil, A. K. Thakur, V. V. Tyagi, A. Sarı and H. M. Ali, *Prog. Energy Combust. Sci.*, 2024, **104**, 101162.

25 Y. Han, Z. Zhang and L. Guo, *Catal. Surv. Asia*, 2020, **24**, 166–177.

26 F. He, W. Li, F. Zhao, X. Zhu, Q. Liu, Z. Liu, X. Zhang and X. Zhang, *Microchem. J.*, 2020, **158**, 105264.

27 Y. Zhao, K. Xia, Z. Zhang, Z. Zhu, Y. Guo and Z. Qu, *Nanomaterials*, 2019, **9**, 455.

28 D. Zhang, J. Cheng, J. Chai, J. Deng, R. Ren, Y. Su, H. Wang, C. Ma, C. S. Lee, W. Zhang, G. P. Zheng and M. Cao, *J. Alloys Compd.*, 2018, **740**, 1067–1076.

29 J. Xuan, Z. Wang, Y. Chen, D. Liang, L. Cheng, X. Yang, Z. Liu, R. Ma, T. Sasaki and F. Geng, *Angew. Chem., Int. Ed.*, 2016, **55**, 14569–14574.

30 L. Sun, J. Xie, L. Zhang, R. Jiang, J. Wu, L. Fan, R. Shao, Z. Chen and Z. Jin, *FlatChem*, 2020, **20**, 100152.

31 X. Zhang, J. Nie, F. Rao, H. Liu, Y. Wang, D. Qu, W. Wu, P. Zhong and G. Zhu, *Ceram. Int.*, 2021, **47**, 31302–31310.

32 S. B. Das, R. K. Singh, V. Kumar, N. Murali and S. Betal, *Bull. Mater. Sci.*, 2024, **47**, 171.

33 K. D. Jayeola, D. S. Sipuka, T. I. Sebokolodi, O. V. Nkwachukwu, C. Muzenda, B. A. Koiki, J. O. Babalola, M. Zhou and O. A. Arotiba, *Chem. Eng. J.*, 2024, **479**, 147482.

34 B. Li, S. Liu, C. Lai, G. Zeng, M. Zhang, M. Zhou, D. Huang, L. Qin, X. Liu, Z. Li, N. An, F. Xu, H. Yi, Y. Zhang and L. Chen, *Appl. Catal., B*, 2020, **266**, 118650.

35 D. Liu, C. Li, J. Ge, C. Zhao, Q. Zhao, F. Zhang, T. Ni and W. Wu, *Appl. Surf. Sci.*, 2022, **579**, 152180.

36 C. Yuan, Z. He, Q. Chen, X. Wang, C. Zhai and M. Zhu, *Appl. Surf. Sci.*, 2021, **539**, 148241.

37 W. Shi, X. Sun, M. Xu, S. Wang, G. Liu and H. Yang, *J. Water Process Eng.*, 2024, **67**, 106229.

38 J. Wan, Q. Liu, P. Tang, Y. Ji, W. Zhong, W. Cheng, X. Xing, X. Lu and L. Zhong, *Analyst*, 2023, **148**, 869–875.

39 Y. Chen, J. Zhang, J. Li, Y. Hu, K. Ge, G. Li and S. Liu, *Anal. Chem.*, 2024, **96**, 2998–3007.

40 J. Low, L. Zhang, T. Tong, B. Shen and J. Yu, *J. Catal.*, 2018, **361**, 255–266.

41 W. Miao, W. He, L. Shen, Y. Li, Z. Fang, Z. Yang and G. Kai, *J. Environ. Chem. Eng.*, 2024, **12**, 114202.

42 Y. Yang, Z. Zeng, G. Zeng, D. Huang, R. Xiao, C. Zhang, C. Zhou, W. Xiong, W. Wang, M. Cheng, W. Xue, H. Guo, X. Tang and D. He, *Appl. Catal., B*, 2019, **258**, 117956.

43 K. Huang, C. Li, H. Li, G. Ren, L. Wang, W. Wang and X. Meng, *ACS Appl. Nano Mater.*, 2020, **3**, 9581–9603.

44 Y. Tang, R. Wang, W. Wang, Y. Lu, X. Jiang, B. Zhao and L. Yang, *ACS Nano*, 2025, **19**, 39384–39397.

45 P. Jiang, L. Zhang, X. Liu, C. Ye, P. Zhu, T. Tan, D. Wang and Y. Wang, *Nat. Commun.*, 2024, **15**, 1010.

46 Y. Tan, H. Jiang, B. Wang and X. Zhang, *New J. Chem.*, 2021, **45**, 19593–19604.

47 J. Wu, L. Qu, Z. Li, L. Zhao, Y. Sun and R. Yang, *Food Chem.*, 2023, **427**, 136672.

48 F. Wang, S. Li, J. Liang, Y. Wang, H. Song, J. Yang, X. Zou and C. Li, *J. Hazard. Mater.*, 2023, **458**, 131954.

49 D. Yang, J. Liu, W. Hu, Y. Xiao, H. Chen, Y. Long and H. Zheng, *Sens. Actuators, B*, 2023, **393**, 134170.

50 S. Wei, C. Zhang and S. Zhang, *Adv. Funct. Mater.*, 2025, e14080.